



High-performance RuO₂/CNT paper electrode as cathode for anion exchange membrane water electrolysis

Jae-Yeop Jeong^{a,b,1}, Jong Min Lee^{c,1}, Yoo Sei Park^d, Song Jin^a, Shin-Woo Myeong^a, Sungjun Heo^a, Hoseok Lee^a, Justin Georg Albers^e, Young-Woo Choi^f, Min Ho Seo^{g,*}, Sung Mook Choi^{a,h,**}, Jooyoung Lee^{a,*}

^a Department of Hydrogen Energy Materials, Surface & Nano Materials Division, Korea Institute of Materials Science (KIMS), Changwon 51508, Republic of Korea

^b Department of Materials Science and Engineering, Pusan National University, Busan 46241, Republic of Korea

^c Republic of KoreaFuel Cell Research & Demonstration Center, Hydrogen Energy Research Division, Korea Institute of Energy Research, Buan-gun 56332, Republic of Korea

^d Department of Advanced Material Engineering, Chungbuk National University, 1 Chungdae-ro, Seowon-gu, Cheongju, Chungbuk 28644, Republic of Korea

^e Fraunhofer Institute for Manufacturing Technology and Advanced Materials IFAM, Winterbergstrasse 28, Dresden 01277, Germany

^f Hydrogen Energy Research Division, Korea Institute of Energy Research, Daejeon 34129, Republic of Korea

^g Department of Nanotechnology Engineering, Pukyong National University, Busan 48547, Republic of Korea

^h Advanced Materials Engineering, University of Science and Technology (UST), Daejeon 34113, Republic of Korea

ARTICLE INFO

Keywords:

Anion Exchange Membrane Water Electrolysis
Cathode
Paper Electrode
Hydrogen Evolution Reaction
Hydrogen Production

ABSTRACT

This study reports on the synthesis and characterization of an effective cathode paper electrode comprising comparatively inexpensive hydrous RuO₂ (h-RuO₂) nanoparticles on carbon nanotubes (CNT) for anion exchange membrane (AEM) water electrolysis. The concentration of hydrous RuO₂ nanoparticles on the CNT was varied to assess their impact on the electrocatalyst for the hydrogen evolution reaction (HER). The electrocatalytic performance of h-RuO₂/CNT comprising 22.0 wt% of Ru was evaluated. Promising results were obtained, with a current density of -10 mA/cm^2 at only 36 mV of overpotential and a mass activity of $-2.41 \text{ A/g}_{\text{Ru}}$ at 100 mV. Additionally, we conducted first-principles calculations to compare the HER catalytic activities of crystalline RuO₂ and hydrous RuO₂ with varying vacancies and to determine the H₂O concentration in the structural lattice using free-energy diagrams. The study findings demonstrate that the h-RuO₂/CNT paper can be used as an efficient electrocatalyst for AEM water electrolysis.

1. Introduction

H₂ is attracting considerable attention as a clean energy resource that can replace conventional fossil fuels. H₂ production via electrochemical water separation is a promising method [1–5]. However, the scarcity and high cost of Pt catalysts typically used in the hydrogen evolution reaction (HER) hamper the production of H₂ [6–9]. To overcome this hurdle, various studies have attempted to develop inexpensive, high-efficiency, and abundant earth element-based electrocatalysts (oxide, sulfide, phosphide, and nitride) to replace Pt [6–11]. However, these materials generally suffer from limited electrochemical activity

and poor durability [12,13]. It has been recently reported that Ru, a platinum group metal with one-third of the cost of Pt, and its oxide RuO₂ exhibit potentially high HER efficiency and stability. However, Ru-based materials are prone to agglomeration because they have a much higher cohesive energy than that of Pt. To solve this problem, Ru-based nanomaterials are uniformly dispersed on a carbon structure, forming catalysts that exhibit HER performance with low overvoltage and excellent durability [14].

Anion exchange membrane (AEM) water electrolysis systems have been developed as alternatives to alkaline water electrolysis (AWE) and proton exchange membrane (PEM) water electrolysis systems. The AEM

* Corresponding authors.

** Corresponding author at: Department of Hydrogen Energy Materials, Surface & Nano Materials Division, Korea Institute of Materials Science (KIMS), Changwon 51508, Republic of Korea.

E-mail addresses: foifrit@pknu.ac.kr (M.H. Seo), akyzaky@kims.re.kr (S.M. Choi), lly5424@kims.re.kr (J. Lee).

¹ These authors contributed equally to this work

water electrolysis system, which combines the advantages of both AWE and PEM water electrolysis systems and excludes their disadvantages, can produce high-purity H_2 by employing an AEM as a solid polymer electrolyte. Various studies have reported improved efficiency and stability of the OER catalyst electrode when IrO_2 is used as the anode in AEM water electrolysis [15–19]. However, the commercialization of such electrocatalysts remains challenging because no HER catalyst electrode has yet been developed that can replace the Pt anode. Hence, it is necessary to develop high-efficiency and cost-effective electrodes for the HER [20,21].

This study describes the fabrication of highly efficient and cost-effective HER paper electrodes for AEM water electrolysis decorated with hydrous RuO_2 nanoparticles on carbon nanotubes (CNT) (h- RuO_2 /CNT). The h- RuO_2 /CNT paper electrode exhibited an overpotential of only 85 mV (with 85% iR compensation) at a current density of -200 mA/cm^2 in 1 M KOH solution. An AEM water electrolysis was constructed by coupling the HER paper electrode to the NiFeCo LDH OER electrocatalyst. Our single-cell AEM water electrolysis achieved a cell voltage of 1.9 V at a current density of only 2.4 A/cm^2 without any iR compensation in 1 M KOH at 50°C , thereby outperforming the Pt/C and NiFeCo LDH catalyst pair by 2.0 A/cm^2 . In addition, our single-cell AEM water electrolysis exhibited a high energy-conversion efficiency of 79.4%.

2. Experimental

2.1. Synthesis of a hydrous RuO_2 on CNT (h- RuO_2 /CNT) electrocatalyst

First, 15 mg of multi-walled CNT (10–20 nm in diameter, $<50\text{ }\mu\text{m}$ in length, Hanhwa Chemical Inc.) was dispersed in 20 mL of deionized (DI) water by conducting ultrasonication for 20 mins to prepare a CNT solution. Next, 10 mL of $x\text{ mmol}$ of a ruthenium chloride ($RuCl_3\cdot H_2O$; $x = 0.01, 0.05, 0.10, 0.15, 0.20\text{ mmol}$; ACROS) solution in DI water was mixed with 20 mL of the CNT solution, heated at 95°C for 18 h, and then cooled down to room temperature. The product was collected by centrifugation, washed several times with ethanol, and the precipitate was dried overnight in an oven at 60°C .

2.2. Fabrication of an h- RuO_2 /CNT paper

One batch of the h- RuO_2 /CNT electrocatalyst and 15 mg of PVA (ACROS) were dispersed in 40 mL of DI water by ultrasonication for 10 mins. The h- RuO_2 /CNT/PVA solution was vacuum-filtered using a Teflon filter and washed several times with ethanol. The resulting paper was dried by blowing N_2 gas and then hot-pressed for 10 mins.

2.3. Characterization

The SEM images were obtained using a JSM-7001 F microscope (JEOL, Tokyo, Japan). The TEM images were captured using a TALOS F200X microscope (Thermo Fisher Scientific, USA). The powder XRD patterns were obtained with a D/MAX 2500 (Rigaku, Japan) diffractometer, equipped with a rotating anode and a $CuK\alpha$ radiation source ($\lambda = 0.15418\text{ nm}$). The XPS spectra were obtained using an ECSA2000 instrument (VG, Microtech) with a dual Mg/Al X-ray source. The wettability of the electrode was characterized by measuring its contact angle with DI water.

2.4. Electrochemical measurements

Polarization curve measurements were performed using a potentiostat (VMP-3, Biologic) in 1 M KOH solution. A carbon rod was used as a counter electrode. A Hg/HgO (in 1 M NaOH solution) electrode was used as a reference electrode. All potentials were converted to potentials versus the reversible hydrogen electrode. Polarization curves for the HER activity were obtained at a scan rate of 5 mV/s with 85% iR

compensation. The synthesized electrocatalyst powder (5 mg) was dispersed in a mixture of 5 wt% Nafion suspension (100 μL ; Sigma–Aldrich) and ethanol (900 μL). Then, the catalyst ink (5 μL) was dropped on a rotating disk electrode (glassy carbon, area: 0.196 cm^2) and dried in an oven at 80°C .

2.5. NiFeCo LDH anode fabrication

The NF was immersed in an aqueous solution containing cobalt acetate tetrahydrate ($Co(CH_3COO)_2\cdot 4H_2O$, ACROS) (33.3 mM) and iron nitrate nonahydrate ($Fe(NO_3)_3\cdot 9H_2O$, ACROS) (66.7 mM) and heated at 95°C for 36 h under magnetic stirring. The electrodes were washed several times with DI water and ethanol and dried overnight in an oven at 60°C .

2.6. Fabrication of an AEM water electrolysis system

The AEM water electrolysis comprised an anode (electrode area: 7.065 cm^2), a cathode (electrode area: 4.9 cm^2), a gas diffusion layer (NF), and an AEM(X37–50 Grade T, Dioxide Materials). The Pt/C and c- RuO_2 /CNT electrocatalysts with a Nafion binder (40 wt%, HISPEC 4000, Johnson Matthey) were used as the cathode and coated on a carbon cloth as a microporous layer (CeTech Co., Ltd.) The loading amount of the electrocatalyst was approximately 1 mg/cm^2 based on the active catalysts. The AEM water electrolysis was supplied as an electrolyte at a flow rate of 50 mL/min in 1 M KOH and operated at 50°C . The AEM water electrolysis test was performed using a potentiostat (BP2C, ZIVE LAB), and its electrochemical performance was analysed based on polarization curve (from 1.3 to $1.9\text{ V}_{\text{cell}}$) measurements. The durability of the AEM water electrolysis system was tested at a constant current of 500 mA/cm^2 . To determine the cell efficiency, the AEM electrolysis power was calculated by multiplying the cell voltage by the current density. The theoretical H_2 production rate at 0.5 A/cm^2 was approximately 0.058 mL/s . The lower heating value (LHV) was used as the H_2 power. The cell efficiency was calculated as follows: (1)

$$\text{Cell efficiency}(\%) = \frac{E_{\text{Output}}}{E_{\text{Input}}} \frac{V_{H_2} \cdot H_0}{W_h} \times 100 \quad (1)$$

W_h : The electric power to produce hydrogen

H_0 : The calorific value of hydrogen ($10.8 \times 10^6\text{ J/m}^3$, lower heating value)

V_{H_2} : The hydrogen gas volume.

2.7. Computational details

DFT calculations were performed using the Vienna ab initio simulation package to elucidate the OER activity of h- RuO_2 [22]. The project-augmented wave pseudopotential was used to replace the interaction of the core electrons [23,24]. The revised Perdew–Burke–Ernzerhof functionals (RPBE) [25] with the generalized gradient approximation (GGA) [26] was employed to describe the exchange–correlation energies of the electrons. The Kohn–Sham wave functions of the valence electrons were expanded using a plane-wave basis set with a cut-off energy of 520 eV. The ionic relaxation step was controlled within a total energy of $1 \times 10^{-4}\text{ eV}$.

To generate a configuration consistent with the degree of hydration of RuO_2 , the primitive cell of RuO_2 was expanded to a $(2 \times 2 \times 2)$ unit cell using the supercell method. A gamma point mesh with $(9 \times 9 \times 9)$ k-points was used to sample the Brillouin zone for the bulk calculation of the RuO_2 unit cell. Following the geometric optimization of RuO_2 , a cluster expansion code was employed to randomly generate configurations corresponding to 0–100% vacancy fraction. Thermodynamically stable structures were determined by calculating the formation energy. A water molecule was then placed at the vacancy site to form h- RuO_2 , as reported by Asta et al. Thereafter, (110) slab models with a vacuum of $20\text{ }\text{\AA}$ were designed in the RuO_2 bulk with hydration degrees of 0, 0.06,

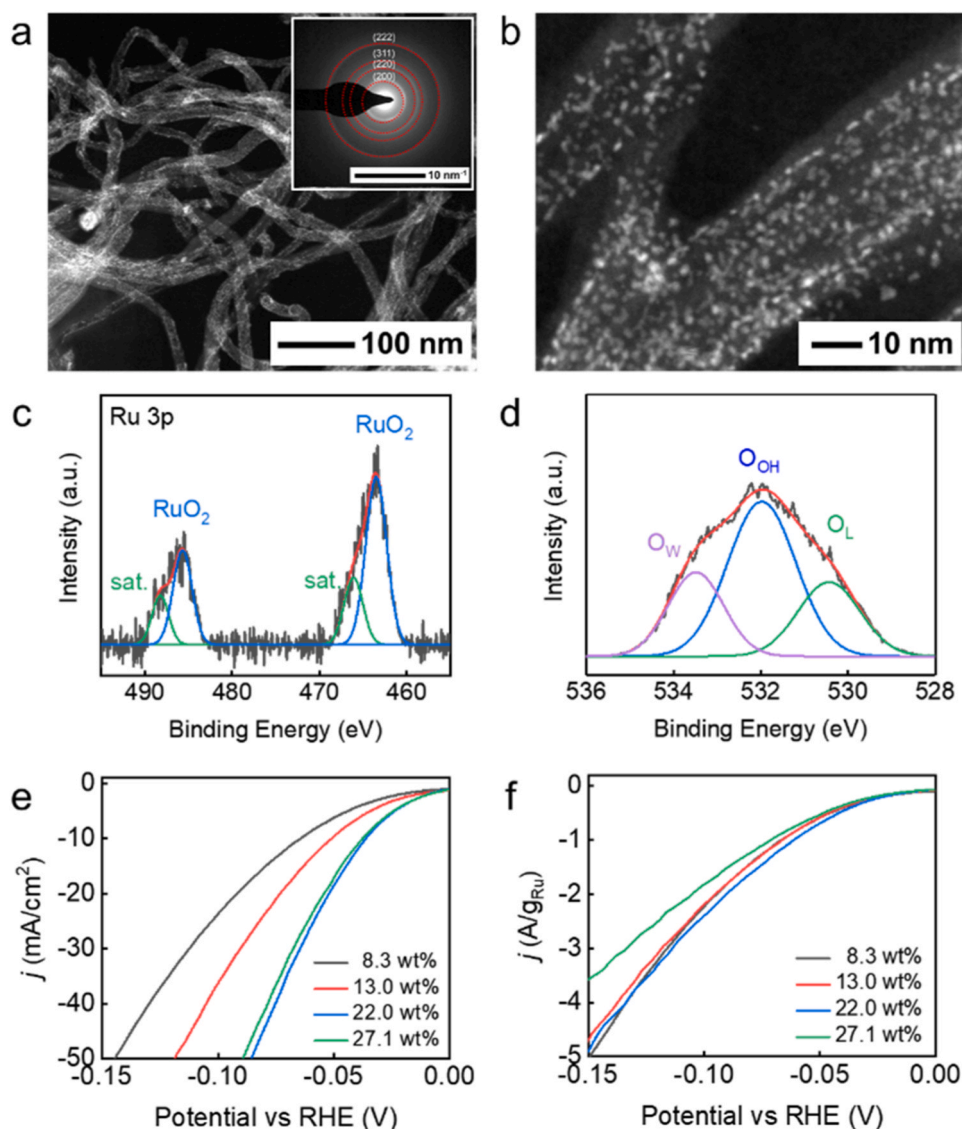


Fig. 1. (a and b) HAADF-STEM image taken from h-RuO₂/CNT-22.0 wt%. Inset shows the SAED pattern of h-RuO₂/CNT-22.0 wt%. (c) Ru 3p core level spectrum, (d) O 1s core level spectrum of h-RuO₂/CNT-22.0 wt%. (e) HER polarization curves and (f) mass-normalized HER polarization curves for h-RuO₂/CNT-x (x=8.3, 13.0, 22.0, 27.1 wt%).

0.13, and 0.19 at%. The k-points were geometrically optimized for each slab. The free energy of the H^{*} intermediates on the stable slab surface was calculated, and the HER activity was predicted for each degree of hydration.

3. Results and discussion

A high-efficiency cathode electrocatalyst consisting of hydrous RuO₂ nanoparticles on carbon nanotubes (CNT) (h-RuO₂/CNT) for AEM water electrolysis was synthesized using a previously reported hydrous RuO₂ (h-RuO₂) nanoparticle synthesis method [27]. High-angle annular dark-field scanning transmission electron microscopy (HAADF-STEM) analysis of the h-RuO₂/CNT showed that the CNT surface comprised 1.7-nm-diameter nanoparticles (Fig. 1a, b, S1 and S2). According to the inductively coupled plasma-mass spectrometry (ICP-MS) analysis, as the concentration of the RuCl₃ precursor was increased to 0.01, 0.05, 0.10, 0.15, and 0.20 mmol, the amount of Ru in h-RuO₂/CNT increased almost constantly to 1.4, 8.3, 13.0, 22.0, and 27.1 wt%, respectively (Fig. S3). When the precursor amount was <0.15 mmol, the CNT were uniformly decorated with hydrous RuO₂ nanoparticles. However, when

it was ≥0.15 mmol, the hydrous RuO₂ nanoparticles tended to aggregate. The selected area electron diffraction (SAED) patterns of the h-RuO₂/CNT contain diffraction rings indexed to the (200), (220), (311), and (222) planes (Fig. 1a, inset). The X-ray diffractometry (XRD) pattern of the electrode showed diffraction peaks at 2θ values of 26.1°, 43.3°, and 54.2° (Fig. S4), which can be indexed to the (002), (101), and (004) reflections of hexagonal graphitic carbon (JCPDS Card No 75-1621), respectively. Elemental mapping showed that RuO₂ nanoparticles were decorated on the CNT (Fig. S5). We further characterized h-RuO₂/CNT using X-ray photoelectron spectroscopy (XPS) [28]. In the Ru 3p core-level spectrum (Fig. 1c), a Ru 3d_{3/2} peak was observed at a binding energy of 463.4 eV, which is in good agreement with the literature value for RuO₂ [28]. In the O 1s spectrum (Fig. 1d), the peaks at 530.5, 531.9, and 533.5 eV correspond to bound lattice oxygen (O_L), hydroxyl (O_{OH}), and chemisorbed water (O_W), respectively. The strongest peak among the O 1s spectral peaks corresponded to the bound hydroxyl group (O_{OH}), indicating that the structure comprised hydrous RuO₂. The C 1s spectrum contained peaks corresponding to C=C(sp²), C-O, C=O, and C-O=O (Fig. S6). We synthesized h-RuO₂ nanoparticles without CNT and performed TGA to determine the wt% of H₂O present

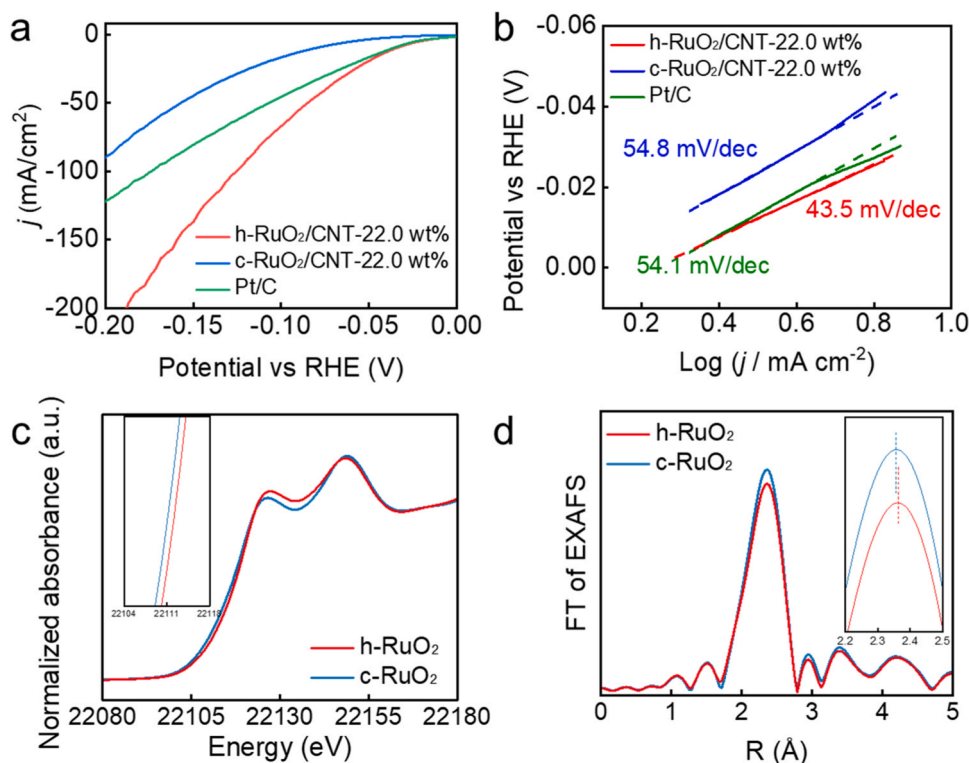


Fig. 2. (a) HER polarization curves and (b) Tafel plots of the h-RuO₂/CNT-22.0 wt%, c-RuO₂/CNT-22.0 wt% and Pt/C electrocatalysts. (c) Normalized Ru K-edge XANES spectra and (d) Ru K-edge FT-EXAFS spectra of the h-RuO₂/CNT-22.0 wt% and c-RuO₂/CNT-22.0 wt%.

in these nanoparticles. The H₂O present in the h-RuO₂ nanoparticles was strongly bonded and was lost only within the 100–300 °C range, confirming that the synthesized h-RuO₂ contained approximately 8.9 wt% of H₂O (Fig. S7). These results indicate that the CNT contained hydrous RuO₂ nanoparticles.

We first investigated the HER performance of h-RuO₂/CNT- x (x = 8.3, 13.0, 22.0, 27.1 wt%) electrocatalysts as a function of Ru content in 1 M KOH at room temperature, which shows the following trends, as determined from the 85% iR -corrected LSV curve: h-RuO₂/CNT-22.0 wt% > h-RuO₂/CNT-27.1 wt% > h-RuO₂/CNT-13.0 wt% > h-RuO₂/CNT-8.3 wt% (Fig. 1e). At a current density of -10 mA/cm², the h-RuO₂/CNT-22.0 wt% electrocatalyst required an overpotential of only 36 mV. To compare and evaluate the HER performance of the catalysts, we calculated their turnover frequency (TOF), which determines the intrinsic electrocatalytic efficiency of HER catalysts. The TOF value of h-RuO₂/CNT- x was 0.25 H₂/s at 100 mV, except for h-RuO₂/CNT-27.1 wt% (0.18 H₂/s) (Fig. S8). In addition, each electrocatalyst was evaluated by normalizing the polarization curve to the Ru mass. The mass activity was observed to be -2.41 A/g_{Ru} at 100 mV, except for h-RuO₂/CNT-27.1 wt% (-1.83 A/g_{Ru}), similar to the TOF result (Fig. 1f). In addition, the catalytic activity was evaluated by determining the electrochemically active surface area (ECSA) using electrochemical double-layer capacitance. The ECSA of the h-RuO₂/CNT- x electrocatalysts increased with the increase in the amount of the h-RuO₂ support (Fig. S9). For a fair comparison of the catalytic activity, the HER polarization curve was normalized by the ECSA. The HER activity of the h-RuO₂/CNT-27.1 wt% electrocatalyst was found to be lower than that of the other h-RuO₂/CNT- x catalysts. Hence, when the Ru content is ≥ 22 wt%, the nanoparticles tend to agglomerate, which decreases the number of active sites present on the catalyst, thereby reducing the activity of Ru. The HER electrocatalytic efficiency of the h-RuO₂/CNT electrocatalysts was demonstrated by performing electrochemical impedance spectroscopy (EIS) to study the electrode kinetics in the HER. The EIS plots show the charge-transfer resistance of the h-RuO₂/CNT- x electrocatalysts

(Fig. S10). Regarding the order of the HER activity, the h-RuO₂/CNT-22.0 wt% and h-RuO₂/CNT-27.1 wt% electrocatalysts delivered an R_{ct} lower than that of the RuO₂/CNT-8.3 wt% and h-RuO₂/CNT-13.0 wt% electrocatalysts, respectively. These results indicate that 22.0 wt% h-RuO₂ nanoparticles decorated on CNT exhibit the most efficient HER catalytic properties.

We also synthesized RuO₂/CNT-22.0 wt% with excellent crystallinity (c-RuO₂/CNT-22.0 wt%) by heat-treating h-RuO₂/CNT-22.0 wt% for comparison with c-RuO₂ (Fig. S11). To compare the HER catalytic activity of the h-RuO₂/CNT-22.0 wt% electrocatalyst, we prepared commercial Pt/C as well as crystalline RuO₂/CNT-22.0 wt% (c-RuO₂/CNT) electrocatalysts through heat treatment. The h-RuO₂/CNT-22.0 wt% electrocatalyst required only 85 mV of overpotential at a current density of -50 mA/cm², which was 22 and 73 mV lower than those required for Pt/C and c-RuO₂/CNT, respectively (Fig. 2a). The Tafel plot reflects the electrochemical kinetics that relates the rate of electrochemical reactions with the overpotentials for the catalyst. The Tafel slope for the h-RuO₂/CNT-22.0 wt% electrocatalyst was 43.5 mV/dec, much lower than that for Pt/C (54.1 mV/dec) and c-RuO₂/CNT (59.0 mV/dec), indicating a higher rate of the HER with the h-RuO₂/CNT-22.0 wt% electrocatalyst (Fig. 2b). To understand the local atomic and coordination numbers of the chemical bonds in h-RuO₂ and c-RuO₂, we performed X-ray absorption near-edge structure (XANES) and X-ray absorption fine structure (EXAFS) measurements. Fig. 2c shows the XANES spectra. The Ru K-edge showed no significant difference between the k-edge energies of h-RuO₂ and c-RuO₂ [29]. However, the features near the edges differed, indicating that the short-range structures of the two ruthenium oxides are different. In contrast, the intensity of the EXAFS qualitatively indicates the coordination number of a chemical bond. Fig. 2d shows that the intensity of the EXAFS spectrum of h-RuO₂ is lower than that of c-RuO₂, indicating an increased degree of structural disorder [30]. Therefore, the HER performance improved by increasing the number of active sites owing to the highly disordered and amorphous structure of h-RuO₂.

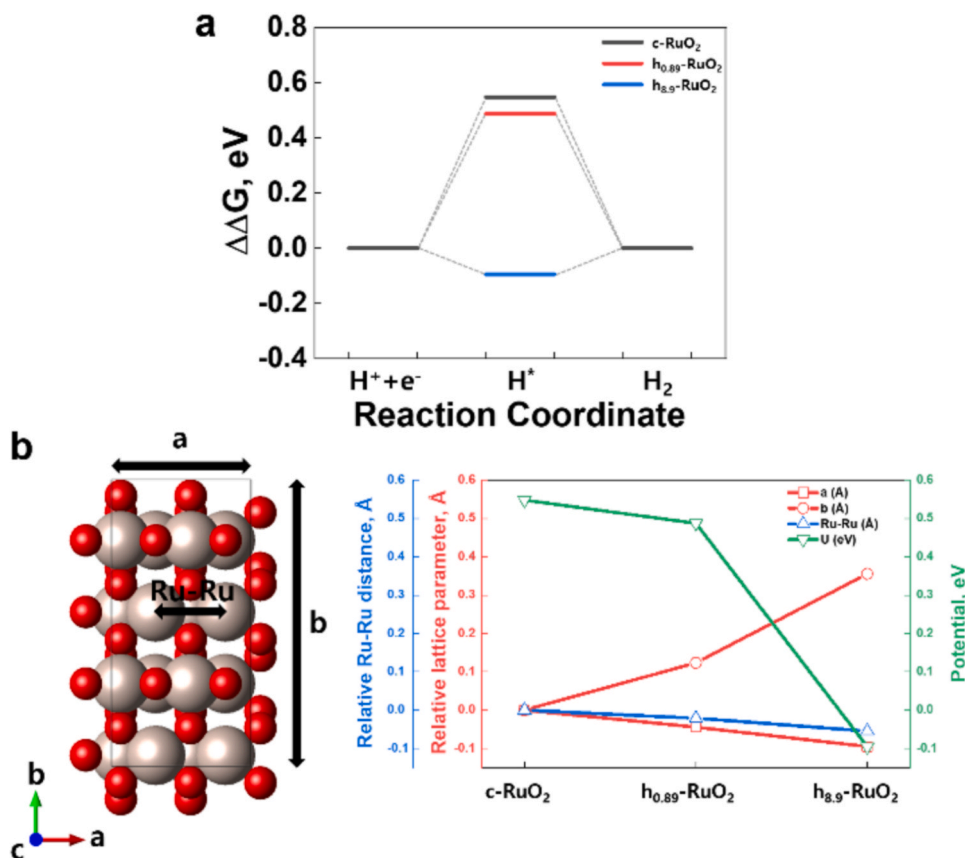


Fig. 3. (a) Free energy diagram for HER of c-RuO₂ and h-RuO₂ and (b) change of lattice parameter and potential change according to degree of hydration.

Next, we conducted a first-principles-based quantum mechanics calculation for a theoretical explanation and to compare the HER catalytic activities of c-RuO₂ (e.g., crystalline RuO₂ shown in Fig. S12) and h-RuO₂. The thermodynamically stable c-RuO₂ with vacancies was also explored as a reference for the P42/mnm space group (ICSD number 15071). The h-RuO₂ catalyst was defined by extending the primitive unit cell of RuO₂ to (2×2×2) by considering the configuration of the injected H₂O molecules in the lattice, as shown in Fig. S13 and S14. The h-RuO₂ catalyst was designed to generate vacancies at its Ru sites, as reported by Asta et al. [31]. To create such RuO₂ structures, defect structures were first randomly generated using a cluster expansion code [32]. Subsequently, geometric optimization was performed using density functional theory (DFT) calculations for the h-RuO₂ catalyst with 0.89 and 8.9 wt% of H₂O. The formation energies were calculated using Eqs.

Where $E_f^{RuO_2}$ is the formation energy, $E(RuO_2)$ is the total DFT energy at the ground state, and μ is the chemical potential. Several reports have described the surface reactions of hydrous RuO₂ crystals [33–35]. For the surface model, the thermodynamically stable h-RuO₂ was generated using bulk models with hydration degrees of 0.89 and 8.9 wt%, denoted as h_{0.89}-RuO₂ and h_{8.9}-RuO₂, respectively. Before calculating the formation energy, three slab models of RuO₂ with the (111), (110), and (100) crystallographic orientations were constructed to evaluate their surface energies. Our analysis revealed that the (110) slab exhibited a stable surface, indicating that it was the most appropriate model for calculating the subsequent formation energies. To determine the HER free energy, we designed a slab model of the previously identified c-RuO₂(110) and h-RuO₂(110), as depicted in Fig. S15.

To compare the electrochemical potentials of the thermodynamically determined spontaneous reactions, it is necessary to understand the HER mechanism on the RuO₂(110) surface. The HER mechanism includes the following three electrochemical reaction steps: the initial state $H^+ + e^-$, the intermediate adsorbed H^* , and the final state $1/2 H_2$, [36] which can

be expressed by the Volmer, Tafel, and Heyrovsky reactions, respectively. The HER activity is theoretically predicted based on the Sabatier principle, which states that the adsorption energy between H^* and the catalyst surface should be neither too strong nor too weak [37–39]. The Gibbs free energy of the hydrogen intermediate state is used to explain the predicted activity of the HER. The overall reaction can be expressed by Eqs. (2) and (3).



Where $*$ denotes adsorption sites. The free energy of the reaction (ΔG_{H^*}) was calculated by Eq. (4)

$$\Delta G_{H^*} = \Delta E_H + \Delta E_{ZPE} - T\Delta S_H \quad (4)$$

Where ΔE , ΔE_{ZPE} , T , and ΔS represent the ground-state energy difference, zero-point energy correction, temperature correction, and entropy correction, respectively. The values of ΔE_{ZPE} and ΔS for the H^* intermediates at 298 K were obtained from the thermodynamic tables reported by Nørskov [40,41].

Fig. 3a shows the free energy of RuO₂(110) as a function of its degree of hydration. The ideal potential for ΔG_{H^*} is zero, indicating that the reaction can be spontaneous even with small overpotentials. The HER activity of c-RuO₂ corresponds to a $|\Delta G_{H^*}|$ of 0.548 eV. As the degree of hydration of RuO₂ increases to 0.89 and 8.9 wt%, the potentials become 0.488 and −0.095 eV, respectively. Hence, it can be suggested that the chemisorption energies for H^* on the surfaces of c-RuO₂ and h_{0.89}-RuO₂ were too weak, resulting in unfavourable H^* adsorption kinetics. Moreover, as the degree of hydration increased, the potential decreased to approximately 0, suggesting that the chemisorption of H^* was more optimized in h_{8.9}-RuO₂ than it was in c-RuO₂ and h_{0.89}-RuO₂.

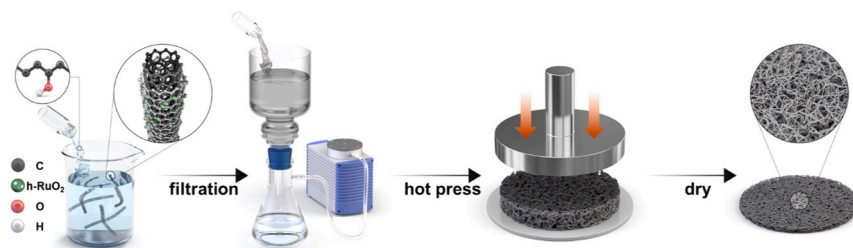


Fig. 4. Fabrication process of h-RuO₂/CNT paper electrode.

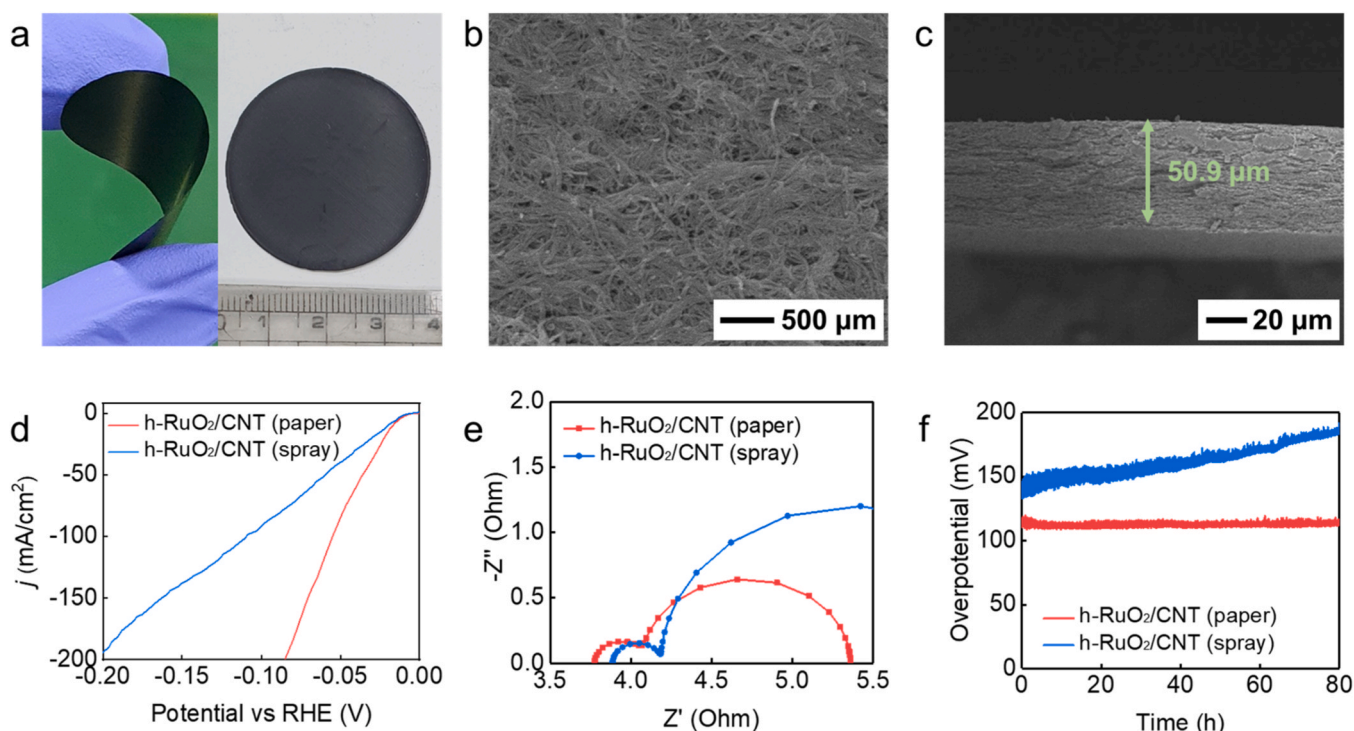


Fig. 5. (a) Photographs of the h-RuO₂/CNT paper electrode. SEM images taken from the (b) top and (c) cross-sections of h-RuO₂/CNT paper. (d) HER polarization curves of the h-RuO₂/CNT paper and h-RuO₂/CNT (spray) electrodes. (e) EIS plot at an applied potential of -0.05 V vs. RHE of the h-RuO₂/CNT paper and h-RuO₂/CNT (spray) electrodes. (f) Chronopotentiometry curve of the h-RuO₂/CNT paper and h-RuO₂/CNT (spray) electrodes at a constant current density of 50 mA/cm² for 80 h.

As the degree of hydration increased, the lattice parameter of h-RuO₂ increased along the b-axis but decreased along the a-axis, as shown in Fig. 3b. This phenomenon decreased the interatomic Ru–Ru distance, which affected the HER activity. Furthermore, as the degree of hydration of RuO₂ increased, the overpotential of the HER on h-RuO₂ decreased. The h_{0.89}-RuO₂ catalyst can undergo a thermodynamically stable electrochemical reaction with a low overpotential, as shown in Fig. 3b.

The water present in RuO₂ induces a geometric effect on c-RuO₂, optimizing the Ru–Ru bond length, which explains the controlled adsorption and desorption strengths using H⁺ intermediates. Consequently, by regulating the degree of hydration, the Ru–Ru interatomic distance can be controlled and electrostructurally modified, leading to an increase in the HER activity. These results are consistent with those obtained by the electrochemical and physicochemical analyses.

We prepared an h-RuO₂/CNT paper catalyst for AEM water electrolysis by filtering the h-RuO₂/CNT-22.0 wt% aqueous dispersion and PVA, followed by hot pressing, as per previously reported methods (Fig. 4) [42]. The optical images of the h-RuO₂/CNT paper catalyst shows its mechanical flexibility (Fig. 5a). Fig. 5b and c show the SEM images of the top and cross-sections of the h-RuO₂/CNT paper. The h-RuO₂/CNT paper was uniformly dispersed without agglomeration and

the formation of a CNT network structure was observed. The mechanical compression of the dried catalyst paper at high temperatures and high pressures produced a $50.9\text{-}\mu\text{m}$ -thick h-RuO₂/CNT paper with a high-density structure. Next, we investigated the electrocatalytic properties of the h-RuO₂/CNT paper electrode for HER. For comparison, we prepared an electrode spray-coated with h-RuO₂/CNT on a carbon cloth. The h-RuO₂/CNT paper electrode showed a highly improved HER activity ($\eta = 85$ mV at 200 mA/cm²) compared to that of the h-RuO₂/CNT (spray) electrode ($\eta = 207$ mV at 200 mA/cm²) (Fig. 5d). Regarding the order of the HER activity, the h-RuO₂/CNT paper electrode delivered an R_{ct} lower than that of the h-RuO₂/CNT (spray) electrode (Fig. 5e). In the case of the h-RuO₂/CNT paper electrode, unlike the h-RuO₂/CNT (spray) electrode, the overpotential required to obtain a current density of -100 mA/cm² did not significantly increase during the measurement for 80 h (Fig. 5f). These results indicate that the h-RuO₂/CNT paper exhibits excellent HER electrode properties owing to its high conductivity and a strong CNT network structure, thereby constituting an integrated electrode.

We constructed an AEM water electrolysis by coupling an h-RuO₂/CNT paper cathode with a NiFeCo LDH/Ni foam anode synthesized by corrosion Fig. S16 and compared its performance with that of an AEM

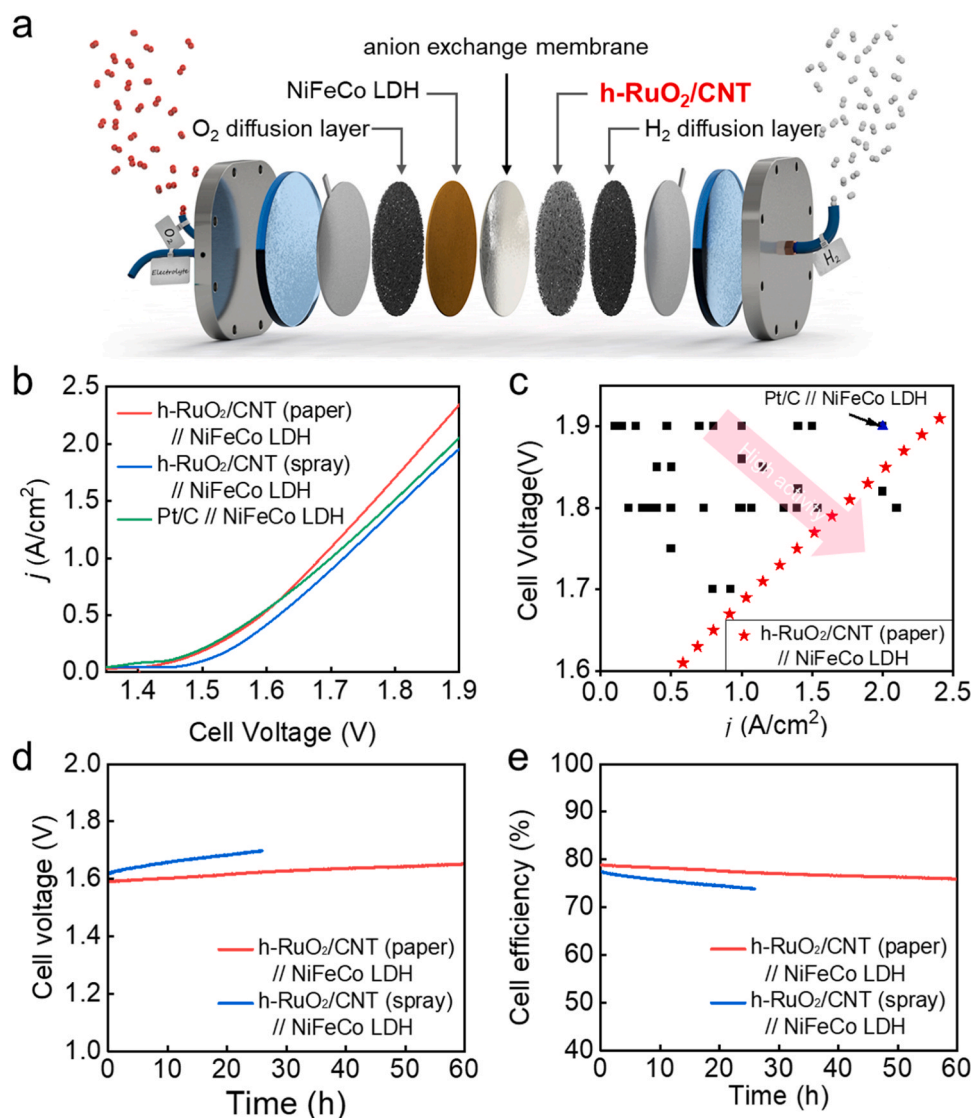


Fig. 6. (a) Schematic representation for an AEM water electrolysis based on $\text{h-RuO}_2/\text{CNT}$ paper and NiFeCo LDH electrode. (b) Polarization curves of three AEM water electrolysis recorded at 50°C in 1 M KOH solution. (c) Comparison of the $\text{NiFeCo h-RuO}_2/\text{CNT}$ paper// NiFeCo LDH AEM water electrolysis with the reported AEM water electrolysis. (d) Chronopotentiometric curve and (e) cell efficiency of the $\text{h-RuO}_2/\text{CNT}$ paper// NiFeCo LDH and $\text{NiFeCo h-RuO}_2/\text{CNT}(\text{spray})//\text{NiFeCo LDH}$ AEM water electrolysis at cell current density of 500 mA/cm^2 .

water electrolysis prepared by pairing a carbon-cloth cathode loaded with a commercial Pt/C catalyst with a NiFeCo LDH anode (Fig. 6a). Fig. 6b shows polarization curves recorded between $1.3\text{ V}_{\text{cell}}$ and $1.9\text{ V}_{\text{cell}}$ at 50°C in 1 M KOH solutions without iR compensation. Our $\text{h-RuO}_2/\text{CNT}$ paper // NiFeCo LDH AEM water electrolysis achieved a cell current density of 2.4 A/cm^2 at $1.9\text{ V}_{\text{cell}}$, higher than that of the Pt/C // NiFeCo LDH AEM water electrolysis (2.0 A/cm^2 at $1.9\text{ V}_{\text{cell}}$) and the $\text{h-RuO}_2/\text{CNT}(\text{spray})$ // NiFeCo LDH AEM water electrolysis (1.9 A/cm^2 at $1.9\text{ V}_{\text{cell}}$). In addition, our AEM water electrolysis required a lower cell voltage to achieve the desired cell current density than that reported in most studies on AEM electrolysis under the same or similar operating conditions (Fig. 6c and Table S1). In our AEM water electrolysis, the cell current density of 0.5 A/cm^2 was achieved by applying only $1.58\text{ V}_{\text{cell}}$ ($\eta = 350\text{ mV}$) across the electrode, which corresponds to a cell efficiency of 79.4% . Hence, it is clear that our AEM water electrolysis outperformed most of the previously reported AEM water electrolysis.

The change in electrical resistance can be determined by electrochemical impedance spectroscopy (EIS). When the $\text{h-RuO}_2/\text{CNT}$ electrode catalyst was prepared as a paper electrode, the electron transfer resistance became much higher than that of the anode prepared by the

coating method (Fig. S17). This is because the catalyst and the electrode were integrally formed, resulting in a network structure between the electrode and the catalyst. The $\text{h-RuO}_2/\text{CNT}$ paper // NiFeCo LDH AEM water electrolysis cell at an applied current density of 0.5 A/cm^2 exhibited a cell voltage of $<1.65\text{ V}_{\text{cell}}$ and a cell efficiency of $>75.9\%$ for 60 h (Fig. 6d and e). The amount of H_2 produced by the AEM water electrolysis was 14.2 mL/min . Constant AEM water electrolysis stability tests were conducted to show that the $\text{h-RuO}_2/\text{CNT}$ paper electrode is highly stable. No noticeable changes were observed in its morphology, structure, reduced Ru loading amount, and chemical state after tests (Fig. S18, S19 and S20). Hence, the $\text{h-RuO}_2/\text{CNT}$ paper can be used to produce highly active electrodes for HER and AEM water electrolysis. Therefore, scaling up our electrolysis could enable the production of H_2 on a large scale with significantly improved efficiency.

4. Conclusion

This paper reports the synthesis and characterization of high-efficiency cathode electrocatalysts comprising hydrous RuO_2 nanoparticles on CNT for AEM water electrolysis. The $\text{h-RuO}_2/\text{CNT}$

electrocatalysts were synthesized using a previously reported method. The nanoparticles were uniformly decorated on the CNT surface. The HER performance of the h-RuO₂/CNT electrocatalyst was investigated as a function of the Ru content of the CNT. We evaluated the electrocatalytic performance of h-RuO₂/CNT with 22.0 wt% of Ru and achieved promising outcomes, with only an overpotential of 36 mV at a current density of -10 mA/cm^2 and a mass activity of $-2.41 \text{ A/g}_{\text{Ru}}$ at 100 mV. In addition, the h-RuO₂/CNT paper // NiFeCo LDH AEM water electrolysis operating in 1 M KOH at 50 °C exhibited a higher performance (2.4 A/cm^2 at $1.9 \text{ V}_{\text{cell}}$) than that of the IrO₂/(Pt/C) AEM water electrolysis.

From a theoretical standpoint, the degree of hydration of RuO₂ nanoparticles greatly affected the HER activity of the electrocatalyst. Specifically, the chemisorption energies of H* on the c-RuO₂ and h_{0.89}-RuO₂ surfaces were too weak, resulting in unfavourable H* adsorption kinetics. However, as the degree of hydration increased, the potential decreased to approximately zero, indicating that the chemisorption of H* was optimized in h_{8.9}-RuO₂. Additionally, the lattice parameter of h-RuO₂ increased with the degree of hydration, decreasing both the interatomic Ru–Ru distance and the HER overpotential. These results suggest that, by regulating the degree of hydration, the interatomic Ru–Ru distance can be controlled and electrostructurally modified, leading to an increase in the activity. The observations presented in the figures are consistent with the electrochemical and physicochemical analyses, providing a strong foundation for further research on RuO₂ nanoparticles for HER applications.

CRedit authorship contribution statement

Hoseok Lee: Formal analysis. **Justin Georg Albers:** Investigation. **Shin-Woo Myeong:** Data curation. **Sungjun Heo:** Data curation. **Song Jin:** Formal analysis, Data curation. **Sung Mook Choi:** Writing – review & editing, Supervision, Investigation, Funding acquisition. **Jae-Yeop Jeong:** Writing – original draft, Visualization, Investigation, Data curation, Conceptualization. **Jooyoung Lee:** Writing – review & editing, Writing – original draft, Investigation, Data curation, Conceptualization. **Jong Min Lee:** Writing – original draft, Formal analysis, Data curation. **Young-Woo Choi:** Formal analysis, Data curation. **Yoo sei Park:** Writing – original draft, Investigation, Formal analysis. **Min Ho Seo:** Writing – review & editing, Formal analysis, Conceptualization.

Declaration of Competing Interest

The authors declare the following financial interests/personal relationships which may be considered as potential competing interests: Sung Mook Choi reports financial support was provided by National Research Foundation of Korea. Sung Mook Choi reports financial support was provided by Rural Development Administration. Sung Mook Choi reports financial support was provided by Korea Institute of Energy Technology Evaluation and Planning. Sung Mook Choi reports financial support was provided by Korea Institute for Advancement of Technology. If there are other authors, they declare that they have no known competing financial interests or personal relationships that could have appeared to influence the work reported in this paper

Data Availability

No data was used for the research described in the article.

Acknowledgements

This work was supported by the National Research Foundation of Korea (NRF) grant funded by the Korea government (MSIT) (No. 2021R1A2C2014348) & "Cooperative Research Program for Agriculture Science and Technology Development (Project No. PJ016253)" Rural Development Administration & the Korea Institute of Energy

Technology Evaluation and Planning (KETEP) and the Ministry of Trade, Industry & Energy (MOTIE) of the Republic of Korea (no. 20218520040040) & the Ministry of Trade, Industry, and Energy (MOTIE), Korea, under "Digital manufacturing platform" (No. P0022331) supervised by the Korea Institute for Advancement of Technology (KIAT).

Appendix A. Supporting information

Supplementary data associated with this article can be found in the online version at doi:10.1016/j.apcatb.2024.124220.

References

- [1] Y. Bai, L. Wilbraham, B.J. Slater, M.A. Zwijnenburg, R.S. Sprick, A.I. Cooper, Accelerated discovery of organic polymer photocatalysts for hydrogen evolution from water through the integration of experiment and theory, *J. Am. Chem. Soc.* 141 (2019) 9063–9071.
- [2] H. Hu, D. Qian, P. Lin, Z. Ding, C. Cui, Oxygen vacancies mediated in-situ growth of noble-metal (Ag, Au, Pt) nanoparticles on 3D TiO₂ hierarchical spheres for efficient photocatalytic hydrogen evolution from water splitting, *Int. J. Hydrog. Energy* 45 (2020) 629–639.
- [3] S. McQueen, J. Stanford, S. Satyapal, E. Miller, N. Stetson, D. Papageorgopoulos, N. Rustagi, V. Arjona, J. Adams, K. Randolph, Department of energy hydrogen program plan, US Department of Energy (USDOE), Washington DC (United States), 2020.
- [4] P.J. Megía, A.J. Vizcaino, J.A. Calles, A. Carrero, Hydrogen production technologies: From fossil fuels toward renewable sources. A mini review, *Energy Fuels* 35 (2021) 16403–16415.
- [5] X. Yan, J. Biemolt, K. Zhao, Y. Zhao, X. Cao, Y. Yang, X. Wu, G. Rothenberg, N. Yan, A membrane-free flow electrolyzer operating at high current density using earth-abundant catalysts for water splitting, *Nat. Commun.* 12 (2021) 4143.
- [6] Z. Kou, K. Wang, Z. Liu, L. Zeng, Z. Li, B. Yang, L. Lei, C. Yuan, Y. Hou, Recent advances in manifold exfoliated synthesis of two-dimensional non-precious metal-based nanosheet electrocatalysts for water splitting, *Small Struct.* 3 (2022) 2100153.
- [7] J. Lai, B. Huang, Y. Chao, X. Chen, S. Guo, Strongly coupled nickel–cobalt nitrides/carbon hybrid nanocages with Pt-like activity for hydrogen evolution catalysis, *Adv. Mater.* 31 (2019) 1805541.
- [8] S. Ye, F. Luo, Q. Zhang, P. Zhang, T. Xu, Q. Wang, D. He, L. Guo, Y. Zhang, C. He, Highly stable single Pt atomic sites anchored on aniline-stacked graphene for hydrogen evolution reaction, *Energy Environ. Sci.* 12 (2019) 1000–1007.
- [9] J. Zhang, Y. Zhao, X. Guo, C. Chen, C.-L. Dong, R.-S. Liu, C.-P. Han, Y. Li, Y. Gogotsi, G. Wang, Single platinum atoms immobilized on an MXene as an efficient catalyst for the hydrogen evolution reaction, *Nat. Catal.* 1 (2018) 985–992.
- [10] Y. Shi, B. Zhang, Recent advances in transition metal phosphide nanomaterials: synthesis and applications in hydrogen evolution reaction, *Chem. Soc. Rev.* 45 (2016) 1529–1541.
- [11] J. Xie, Y. Xie, Transition metal nitrides for electrocatalytic energy conversion: opportunities and challenges, *Chem. – A Eur. J.* 22 (2016) 3588–3598.
- [12] Y. Feng, S. Zhang, L. Zhu, G. Li, N. Zhao, H. Zhang, B.H. Chen, Reduced graphene oxide-supported ruthenium nanocatalysts for highly efficient electrocatalytic hydrogen evolution reaction, *Int. J. Hydrog. Energy* 47 (2022) 39853–39863.
- [13] X.P. Fu, K.Z. Sun, X. Li, H.G. Xu, F. Mao, H. Yang, P.F. Liu, Ruthenium and Iron Co-doped Molybdenum Carbide as a Stable Hydrogen Evolution Electrocatalyst in Harsh Electrolyte, *Chem. – A Eur. J.* (2023) e202302398.
- [14] L. Zhang, H. Jang, Y. Wang, Z. Li, W. Zhang, M.G. Kim, D. Yang, S. Liu, X. Liu, J. Cho, Exploring the dominant role of atomic- and nano-ruthenium as active sites for hydrogen evolution reaction in both acidic and alkaline media, *Adv. Sci.* 8 (2021) 2004516.
- [15] M.J. Jang, J. Yang, J. Lee, Y.S. Park, J. Jeong, S.M. Park, J.-Y. Jeong, Y. Yin, M.-H. Seo, S.M. Choi, Superior performance and stability of anion exchange membrane water electrolysis: pH-controlled copper cobalt oxide nanoparticles for the oxygen evolution reaction, *J. Mater. Chem. A* 8 (2020) 4290–4299.
- [16] C.-Y. Kwon, J.-Y. Jeong, J. Yang, Y.S. Park, J. Jeong, H. Park, Y. Kim, S.M. Choi, Effect of copper cobalt oxide composition on oxygen evolution electrocatalysts for anion exchange membrane water electrolysis, *Front. Chem.* 8 (2020) 600908.
- [17] J. Lee, H. Jung, Y.S. Park, N. Kwon, S. Woo, N.C.S. Selvam, G.S. Han, H.S. Jung, P. J. Yoo, S.M. Choi, Chemical transformation approach for high-performance ternary NiFeCo metal compound-based water splitting electrodes, *Appl. Catal. B: Environ.* 294 (2021) 120246.
- [18] J. Lee, H. Jung, Y.S. Park, S. Woo, N. Kwon, Y. Xing, S.H. Oh, S.M. Choi, J.W. Han, B. Lim, Corrosion-engineered bimetallic oxide electrode as anode for high-efficiency anion exchange membrane water electrolyzer, *Chem. Eng. J.* 420 (2021) 127670.
- [19] J. Lee, H. Jung, Y.S. Park, S. Woo, J. Yang, M.J. Jang, J. Jeong, N. Kwon, B. Lim, J. W. Han, High-efficiency anion-exchange membrane water electrolyzer enabled by ternary layered double hydroxide anode, *Small* 17 (2021) 2100639.
- [20] M.A.R. Anjum, H.Y. Jeong, M.H. Lee, H.S. Shin, J.S. Lee, Efficient hydrogen evolution reaction catalysis in alkaline media by all-in-one MoS₂ with multifunctional active sites, *Adv. Mater.* 30 (2018) 1707105.

- [21] W. Li, G. Cheng, S. Peng, M. Sun, S. Wang, S. Han, Y. Liu, T. Zhai, L. Yu, Tuning hydrogen binding energy by interfacial charge transfer enables pH-universal hydrogen evolution catalysis of metal phosphides, *Chem. Eng. J.* 430 (2022) 132699.
- [22] G. Kresse, J. Furthmüller, Efficient iterative schemes for ab initio total-energy calculations using a plane-wave basis set, *Phys. Rev. B* 54 (1996) 11169.
- [23] P.E. Blöchl, Projector augmented-wave method, *Phys. Rev. B* 50 (1994) 17953.
- [24] G. Kresse, D. Joubert, From ultrasoft pseudopotentials to the projector augmented-wave method, *Phys. Rev. B* 59 (1999) 1758.
- [25] B. Hammer, L.B. Hansen, J.K. Nørskov, Improved adsorption energetics within density-functional theory using revised Perdew-Burke-Ernzerhof functionals, *Phys. Rev. B* 59 (1999) 7413.
- [26] G. Kresse, J. Furthmüller, Efficiency of ab-initio total energy calculations for metals and semiconductors using a plane-wave basis set, *Comput. Mater. Sci.* 6 (1996) 15–50.
- [27] J. Lee, S.A.S. Shah, P.J. Yoo, B. Lim, Hydrous RuO₂ nanoparticles as highly active electrocatalysts for hydrogen evolution reaction, *Chem. Phys. Lett.* 673 (2017) 89–92.
- [28] W. Wang, S. Guo, I. Lee, K. Ahmed, J. Zhong, Z. Favors, F. Zaera, M. Ozkan, C. S. Ozkan, Hydrous ruthenium oxide nanoparticles anchored to graphene and carbon nanotube hybrid foam for supercapacitors, *Sci. Rep.* 4 (2014) 4452.
- [29] D.A. McKeown, P.L. Hagans, L.P. Carette, A.E. Russell, K.E. Swider, D.R. Rolison, Structure of hydrous ruthenium oxides: implications for charge storage, *J. Phys. Chem. B* 103 (1999) 4825–4832.
- [30] Y. Wang, H. Li, W. Zhou, X. Zhang, B. Zhang, Y. Yu, Structurally disordered RuO₂ nanosheets with rich oxygen vacancies for enhanced nitrate electroreduction to ammonia, *Angew. Chem.* 134 (2022) e202202604.
- [31] V. Ozolins, F. Zhou, M. Asta, Ruthenium-based electrochemical supercapacitors: insights from first-principles calculations, *Acc. Chem. Res.* 46 (2013) 1084–1093.
- [32] B. Han, A. Van der Ven, G. Ceder, B.-J. Hwang, Surface segregation and ordering of alloy surfaces in the presence of adsorbates, *Phys. Rev. B* 72 (2005) 205409.
- [33] K.-M. Lin, K.-H. Chang, C.-C. Hu, Y.-Y. Li, Mesoporous RuO₂ for the next generation supercapacitors with an ultrahigh power density, *Electrochim. Acta* 54 (2009) 4574–4581.
- [34] T. Liu, W.G. Pell, B.E. Conway, Self-discharge and potential recovery phenomena at thermally and electrochemically prepared RuO₂ supercapacitor electrodes, *Electrochim. Acta* 42 (1997) 3541–3552.
- [35] J. Rishpon, S. Gottesfeld, Resolution of fast and slow charging processes in ruthenium oxide films: an AC impedance and optical investigation, *J. Electrochem. Soc.* 131 (1984) 1960.
- [36] J.K. Nørskov, T. Bligaard, A. Logadottir, J. Kitchin, J.G. Chen, S. Pandalov, U. Stimming, Trends in the exchange current for hydrogen evolution, *J. Electrochem. Soc.* 152 (2005) J23.
- [37] Y. Bing, H. Liu, L. Zhang, D. Ghosh, J. Zhang, Nanostructured Pt-alloy electrocatalysts for PEM fuel cell oxygen reduction reaction, *Chem. Soc. Rev.* 39 (2010) 2184–2202.
- [38] N. Ramaswamy, U. Tylus, Q. Jia, S. Mukerjee, Activity descriptor identification for oxygen reduction on nonprecious electrocatalysts: linking surface science to coordination chemistry, *J. Am. Chem. Soc.* 135 (2013) 15443–15449.
- [39] M.H. Seo, H.W. Park, D.U. Lee, M.G. Park, Z. Chen, Design of highly active perovskite oxides for oxygen evolution reaction by combining experimental and ab initio studies, *ACS Catal.* 5 (2015) 4337–4344.
- [40] P. Atkins, J. De Paula, *Physical chemistry*, Macmillan, 2006.
- [41] J.K. Nørskov, J. Rossmeisl, A. Logadottir, L. Lindqvist, J.R. Kitchin, T. Bligaard, H. Jonsson, Origin of the overpotential for oxygen reduction at a fuel-cell cathode, *J. Phys. Chem. B* 108 (2004) 17886–17892.
- [42] G.-H. Lim, S. Woo, H. Lee, K.-S. Moon, H. Sohn, S.-E. Lee, B. Lim, Mechanically robust magnetic carbon nanotube papers prepared with CoFe₂O₄ nanoparticles for electromagnetic interference shielding and magnetomechanical actuation, *ACS Appl. Mater. Interfaces* 9 (2017) 40628–40637.